ATMOSPHERIC RE-ENTRY ANALYSIS OF SOUNDING ROCKET PAYLOADS

Andreas Stamminger[1]

[1] *Deutsches Zentrum für Luft- und Raumfahrt (DLR), RB-MR, Oberpfaffenhofen, D-82234 Wessling, Germany,
Tel.: +49-8153-28-2616, Fax:+49-8153-28-1344, Email: andreas.stamminger@dlr.de*

ABSTRACT

The atmospheric re-entry of sounding rocket payloads is an important phase of the ballistic flight, especially when instruments and experiments shall be recovered for future flights or interpretation of experiment data. The understanding of the dynamic behaviour of cylindrical and cone-cylindrical payloads during the re-entry is a prerequisite to ensure a successful deployment of the parachute system. This includes not only the knowledge of the payload vehicle attitude and rate data but also the "global view" on deceleration, descent time and terminal recovery velocity. The paper describes the analysis work that has been conducted at the Mobile Rocket base of the German Aerospace Center (DLR) on flight data of several TEXUS and MAXUS payloads that have been reviewed and compared.

1. INTRODUCTION

A detailed examination of the re-entry of sounding rocket payloads became necessary during the development of the SHarp Edged Flight EXperiment SHEFEX which was launched in October 2005 from Andøya Rocket Range, Norway [18], [20]. During the experiment phase from 90 km down to 20 km the payload remained attached to the burnt-out 2nd stage motor to provide a stable flight. At an altitude of 14 km the motor was separated from the payload module which was then highly unstable with a centre of gravity near the geometric centre. The payload module started to tumble and decelerate very quickly. During the layout of the vehicle, the final recovery velocity had been detected as a possible critical design point because the vehicle needed to decelerate from a velocity of around 1700 m/s before the separation, to a moderate velocity for the recovery parachute deployment at an altitude of approximately 4 km. The parachute system was designed for a maximum recovery velocity of 230-280 m/s which is around double the velocity of standard payloads, such as TEXUS, MAXUS or MASER payloads. The flight showed that this design criterion is not too critical as the payload starts to take up an attitude with an angle of attack of approximately 90° which means that the flow direction is lateral around the payload. Another critical criterion became obvious during separation. Due to the higher drag, an enormous deceleration peak of more than 70 g appeared and the pressure in the manifold ring increased which activated the baroswitch for the recovery sequence prematurely.

Because of the payload velocity which was still greater than 1500 m/s, the parachute system failed. This example showed that a better understanding of payload re-entry motion and drag coefficient is necessary, especially for vehicles in non-standard ballistic flights.

2. RE-ENTRY PAYLOAD CONFIGURATIONS

Sounding rocket payloads are usually cylindrical or cone-cylindrical bodies containing modules for experiments, all necessary service systems and recovery. During re-entry all considered payloads have a cylindrical shape, because the nose cone is separated after burn-out of the last stage. The payloads differ in diameter D_{PL}, 0.438 m for TEXUS and 0.64 m for MAXUS, but the ratio of length L_{PL} to diameter D_{PL} is comparable. The following figure shows some of the analyzed payloads.
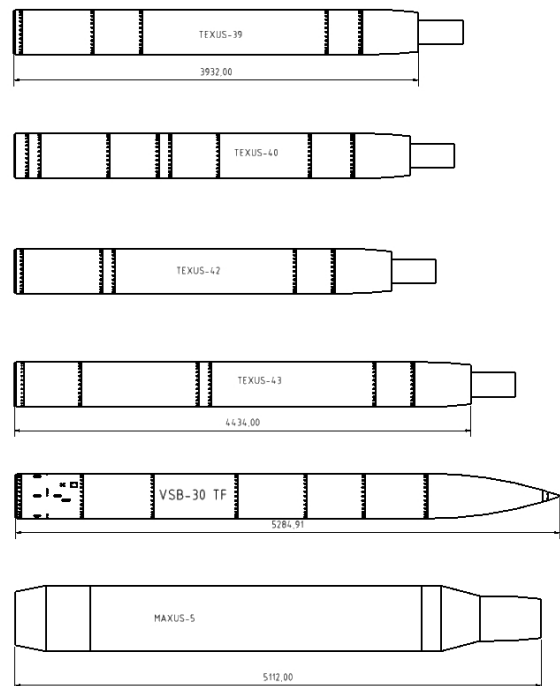

Figure 1. Payload Re-Entry Configuration of TEXUS-39, 40, 42, 43, VSB-30 TF and MAXUS-5

The payload ratio length to diameter differs from $\frac{L_{PL}}{D_{PL}} = 7.88$ (MAXUS-7) to $\frac{L_{PL}}{D_{PL}} = 10.12$ (TEXUS-43). The TEXUS payloads in Figure 1 are shown with the nose cone ejection can that is connected with the heat

shield until the aerodynamic loads increase during re-entry and it bursts off.

The considered TEXUS payload re-entry mass m_{PL} differs from 361 kg [9] to 397 kg [10]. The MAXUS payloads re-entry mass m_{PL} differs from 704 kg to 729 kg [2].

To avoid a stable re-entry, the centres of gravity of these payloads coincide with the longitudinal aerodynamic centres. As an example, the following figure shows the TEXUS-43 payload.
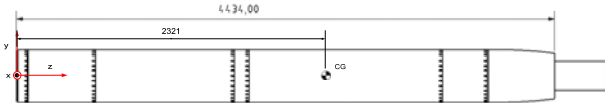

Figure 2. TEXUS-43 Re-entry Configuration with Nose Cone Ejection Can

Referenced to the payload length L_{PL} the TEXUS-43 centre of gravity is placed 52 % from the separation plane. The distance between centre of gravity $z_{BF,cg}$ and aerodynamic centre $z_{BF,cp}$ referenced to the payload length L_{PL} is around 2 % which is more distant than for TEXUS payloads that have been launched before.

This distance considerably influences the payload motion during re-entry. For the analysis of the vehicle attitude during the atmospheric entry it is important to take a look at the arrangement of antennae or other protuberances as it is illustrated in Figure 3. The x_{BF}-Axis (Yaw-Axis) builds the position. Eight hook antennae are positioned on the payload. The telecommand-antennae, which influence the orientation of payload in the flow field the most, are placed on the position $Pos_{Telecommando} = 55°$ and opposed on 235°.
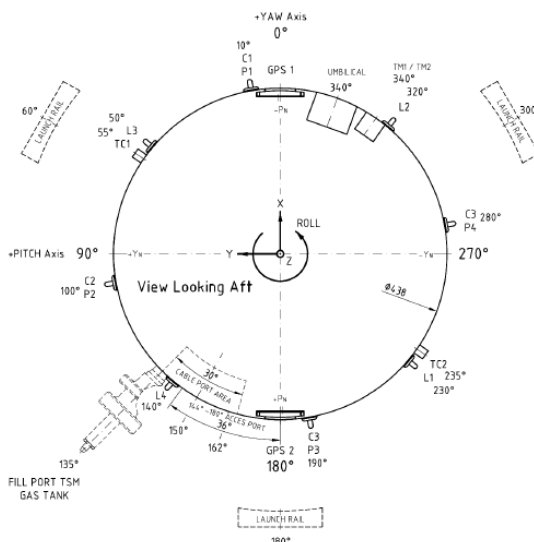

Figure 3. TEXUS-43 Paylaod Cross-Section View contrary to launch direction [16]

3. AERODYNAMIC DRAG

The primary force on a payload during the re-entry, the aerodynamic drag, is aligned with the payload flight direction v_{VCVF}. For symmetrical vehicles like usual sounding rocket payloads with a high flight path angle γ_{VCVF} during the ballistic entry into atmosphere, the lift force is smaller than drag by a factor of 10.

3.1. Drag Coefficient Definition

First considerations on flow resistance were made by Isaac Newton with the scientific output that the drag is proportional to the fluid density ρ, the square of the velocity v_{VCVF}^2 and the projected Area A.

As it was shown later, this was wrong concerning the proportional factor, which is not only dependent on size and configuration of the projected frontal area but also the complete body form [21].

However the Newton theory condition of a fluid of non-interacting molecules is satisfied if the intermolecular forces are small compared to the inert forces on the molecule, as it is the case for free molecular flow when space between the fluid molecules is large. This can be assumed for sounding rocket payloads at higher altitudes. A measurement for the space between these molecules is the Knudsen Number Kn,

$$Kn = \frac{\lambda}{D_{PL}} \qquad (1)$$

where λ is mean free path and the characteristic length is the payload diameter D_{PL} because a lateral incoming flow on the payload is assumed. The region $Kn < 0.01$ is called continuum flow. Free molecular flow is defined by a Knudsen-Number $Kn > 10$ [11] which is a flow region that is less important for the re-entry of sounding rocket payloads, because a significant measurement of drag is limited to an altitude of 120 km.
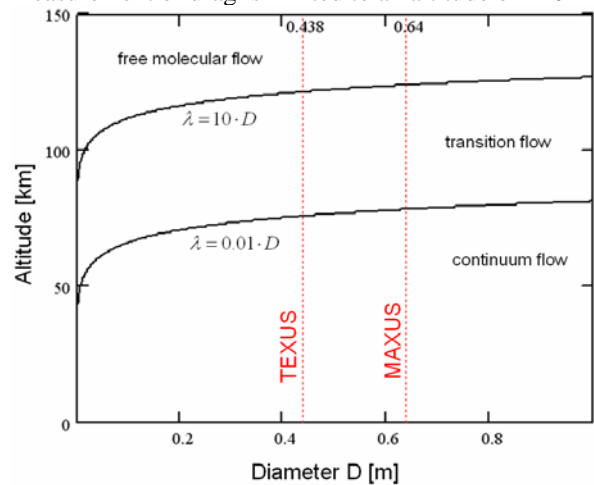

Figure 4. Flow Regime, Assuming Lateral Incoming Flow on the Payload

Experiments of Ludwig Prandtl and Gustave Eiffel showed that the flow resistance is determined by the complete shape of the body. The Newton theory had to be extended with the use of a drag number ς_D that describes the body shape and the factor ½ to abide a continuing notation in aerodynamic equations [15], yielding to the well known equation:

$$F_{Drag} = \varsigma_D \cdot \frac{\rho}{2} \cdot u_\infty^2 \cdot A \qquad (2)$$

The drag number ς_D is therefore referenced to the projected area A however the drag coefficient c_D is based on a certain reference area A_{ref}. The regarded reference areas during this analysis are the payload cross section $A_\bigcirc = \frac{\pi}{4} \cdot D_{PL}^2$ and the payload longitudinal section $A_\square = D_{PL} \cdot L_{PL}$. The referenced drag coefficient is $c_{D,\bigcirc}$, respectively referenced to the longitudinal section $c_{D,\square}$.

3.2. Drag Influencing Parameters

Usually estimations for drag coefficients are based on theoretical data and measurements of a cylinder shape in wind tunnels under certain conditions. The two dimensionless similarity indicators that describe the flow field condition and affect the drag coefficient in the continuum mechanics are the Mach-Number Ma and the Reynolds-Number Re.

3.2.1 Reynolds-Number
The Reynolds-Number describes the boundary layer thickness. With a higher viscosity ν of a fluid, a increase of turbulence diffusion can be observed and the boundary layer thickness increases. It decreases with increasing flow velocity [8], [21].

$$Re = \frac{v_{VCVF} \cdot D_{PL}}{\nu} = \frac{\rho \cdot v_{VCVF} \cdot D_{PL}}{\eta} \qquad (3)$$

Before taking a look at flight data of TEXUS and MAXUS payloads, Figure 1 shows the theoretical drag coefficient $c_{D,\square}$ for a cylinder in a lateral flow field depending on the Reynolds-Number.
Two regions are noticeable, one for $300 < Re < 300000$ and the other region is $Re > 300000$. Now a closer look is taken on the different regions and in which altitudes they occur during a re-entry of a typical sounding rocket payload. All altitude data refer to TEXUS payloads. For a MAXUS payload the Reynolds-regions are shifted in higher altitudes by a few kilometers.

3.2.1.a   Reynolds-Number $Re \leq 4$
In this region the curve decreases precipitously and an analytic solution for the drag coefficient exists [12], [8],

[21]. For sounding rocket payloads this region appears only at an altitude $h_{ECEF} > 110$ km.
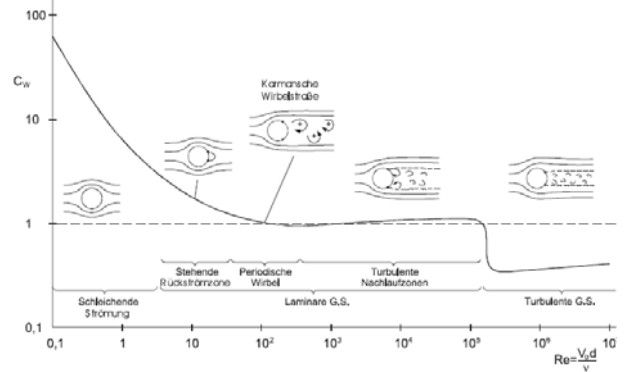

Figure 5. Drag Coefficient $c_{D,\square}$ of a rectangular cylinder vs. the Reynolds-Number [8]

3.2.1.b   Reynolds-Number $4 \leq Re \leq 40$
The inert forces influence on the drag coefficient increases and the flow starts to separate behind the payload. For TEXUS payloads this region appears in altitudes of 110 km to 100 km.

3.2.1.c   Reynolds-Number $40 \leq Re \leq 300$
At an altitude between 100 km and 85 km the Reynolds-Number of flow field around the payload is in the region $40 \leq Re \leq 300$. The laminar boundary layer starts to increase and a periodic separation of the flow field on the cylindrical body can be observed, a phenomenon called Kármán vortex stream [8], [21].

3.2.1.d   Reynolds-Number $300 \leq Re \leq 300000$
In this Reynolds-Number region the boundary layer separates at the cylinder vertex but the appearing vortexes are not stable and a turbulent wake with the size of the payload diameter D_{PL} occurs. In this Reynolds-region usually a drag coefficient of $c_{D,\square} = 1.2$ is assumed [8], [1]. This flow field condition occurs during the re-entry of a payload in an altitude of 85 km to 37 km.

3.2.1.e   Reynolds-Number $Re \geq 300000$
In this Reynolds-region a sudden drop by a factor 2 to 4 of the drag coefficient $c_{D,\square}$ can be observed, followed by a slowly increase of the drag coefficient with increasing Reynolds-Number. The different factors of the drop can be found in [21], [8] and [1], always regarding that it is also dependent on the flow field Mach-Number. This flow field condition appears during the re-entry of the payload after passing an altitude of 37 km.

3.2.2 Mach-Number
The Mach Number describes the flow velocity referenced to the local speed of sound. The Mach-

Number Ma has a physical significance because frictionless flows of compressible fluids are comparable if the Mach-Number Ma and the adiabatic exponent κ are similar [21].

The continuum flow, the flow regime that is significant for the re-entry of sounding rocket payloads (see also Figure 4), can be characterized dependent on the Mach-Number [7]:

- $Ma \leq 0.3$: Incompressible Flow
- $0.3 < Ma < 1.0$: Compressible Flow
- $0.8 < Ma < 1.2$: Transonic Flow
- $Ma < 1.0$: Supersonic Flow
- $Ma > 5.0$: Hypersonic Flow

The drag coefficient changes rapidly in the Mach-region around $Ma \approx 1$ and measurements of the drag coefficient in the transonic flow in a laboratory are subjected to large uncertainties [13]. Empirical data for the drag coefficient $c_{D,\square}$ for Mach-Numbers $Ma > 0$ to $Ma < 2.2$ can be found in [1] and [14]. Maximum drag coefficients are around $c_{D,\square} \approx 1.8$ at Mach-Numbers little lower than 1. Depending on a subcritical or supercritical flow, which is given for the re-entry of sounding rocket payloads, the drag coefficient curve drops to $c_{D,\square} \approx 0.3$, see also chapter 3.2.1.e.

3.2.3 Knudsen-Number and other Parameters

Another parameter that can describe the drag behaviour of a payload is the already mentioned Knudsen-Number. At an altitude of 120 km the TEXUS or MAXUS payload is exposed free molecular flow, and the usually used drag number ς_D for a cylindrical body differs from $\varsigma_D = 2.0$ [15] to $\varsigma_D = 3.0$ [3]. Other parameter like payload length and surface roughness are described in [21], [4], [8].

4. EMPIRICAL DRAG COEFFICIENT CALCULATION

During the analysis of the re-entry of the sounding rocket payloads, drag coefficients based on empirical data have been calculated. The availability of accurate GPS and sensor data supported to analyze the acceleration of the payload from 120 km on the descent. With the use of gravitation models the acceleration is reduced to its aerodynamic component only.

$$\vec{a}_{ECEF,aero} = \ddot{\vec{r}}_{ECEF} - \vec{a}_{ECEF,grav} \quad (4)$$

The atmospheric drag is only the part of the aerodynamic acceleration that is contrary to the relative velocity vector including wind velocities. The drag coefficient can be calculated with

$$c_D = -2 \cdot a_{drag} \cdot \frac{m_{PL}}{A_{ref} \cdot \rho \cdot v_{rel}^2} \quad (5)$$

Next to acceleration data and position of the payload knowledge of the local gravitation and atmosphere is necessary. During this analysis, gravitation is calculated with the Joint Gravity Model JGM-3, an Earth geopotential model, complete to spherical degree and order 70 [6], [15]. For the calculation of the atmosphere density, three atmosphere models dependent on altitude have been used.

- $h_{ECEF} \leq 20$ km : US Standard Atmosphere 1976
- 20 km $< h_{ECEF} < 120$ km : CIRA86
- 120 km $< h_{ECEF}$: Harris-Priester Density Model

5. TYPICAL PAYLOAD RE-ENTRY

Vehicles, where the centre of gravity coincides with the longitudinal aerodynamic centre, as it is the case for TEXUS, MAXUS and MASER payloads, are usually spun-up about the longitudinal axis before re-entry into the atmosphere to eliminate concentration of surface aerodynamic heating and enhance the condition for flat spin [19]. Analysis of flight data has shown that the payload spinning stops when dynamic pressure starts to build and it is stabilized to one lateral position depending on protuberances like telecommand- or S-band-antennae, before the payload reaches the flight time with maximum deceleration.
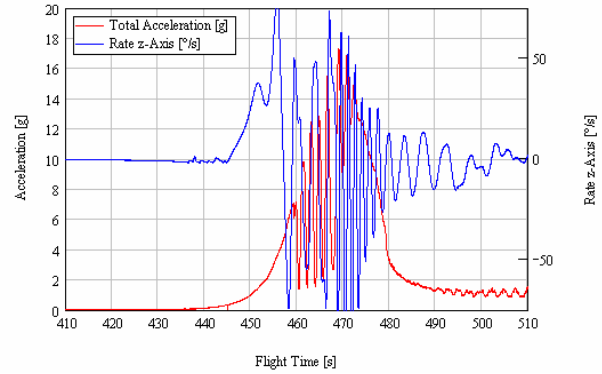

Figure 6. TEXUS-43 – Total Acceleration a_{BF} and Spin-Rate $\dot{p}$ vs. Flight Time t during re-entry

E.g. in Figure 6, the TEXUS-43 has been spun up at an altitude $h_{ECEF} \approx 60$ km to a maximum spin rate $\dot{p} \approx 82 \frac{°}{s}$ but the roll motion stops at an altitude of 38 km after nearly 12 seconds with less than one full payload revolution. At this flight time the payload has reached one third of its maximum deceleration peak $a_{BF} \approx 13$ g. The MAXUS-7 payload has been spun up in higher altitude of 81 km and reaches therefore a 3 times higher spin rate but the telecommand-antennae stabilize the payload 16 s later at an altitude of 37 km, which is around 3 s before the maximum deceleration of 36 g.
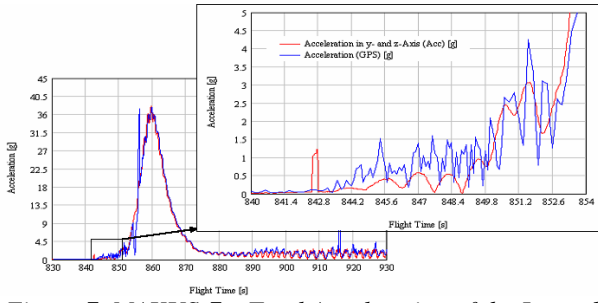
Figure 7. MAXUS-7 – Total Acceleration of the Lateral Axis (Accelerometer-Data) and Total Acceleration (GPS Data) vs. Flight Time during Re-entry

If acceleration data of GPS and the lateral accelerometers are compared, conclusions on the attitude of the payload are possible. If both curves coincide, the payload has an attitude that is perpendicular to the incoming flow. This applies to the re-entry behaviour of the MAXUS-7 payload (see Figure 7), also the difference in acceleration data at higher altitudes indicates that the payload enters the higher atmosphere slightly with the re-entry cone ahead. If the bodyfixed acceleration data is not disturbed by roll rotation or flat spin motion, it is also possible to calculate a pseudo angle of attack σ. For a very stable period with an pseudo angle of attack $\sigma = -1°$ this is shown for the MAXUS-7 payload in Figure 8.
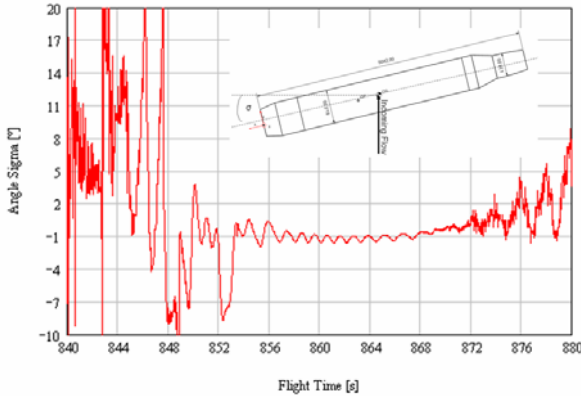

Figure 8. MAXUS-7 - Angle σ during Re-entry till Beginning of the Flat Spin

As already mentioned payloads stop the roll motion with the increase of aerodynamic loads and stabilize to a lateral position between the telecommand-antennae. Figure 9 shows the position $Pos_{AeroFlow}$ for the TEXUS-43 before and after the roll motion. It adopts a position $Pos_{AeroFlow} \approx 322°$ referring to the cross section in Figure 3. In addition, this incoming flow is indicated by the temperature sensors on the payload structure [16]. The MAXUS-7 payload is also stabilized between the telecommand-antennae and traces of ablation can be found also on the recovered payload structure at the position that is indicated by the acceleration data.
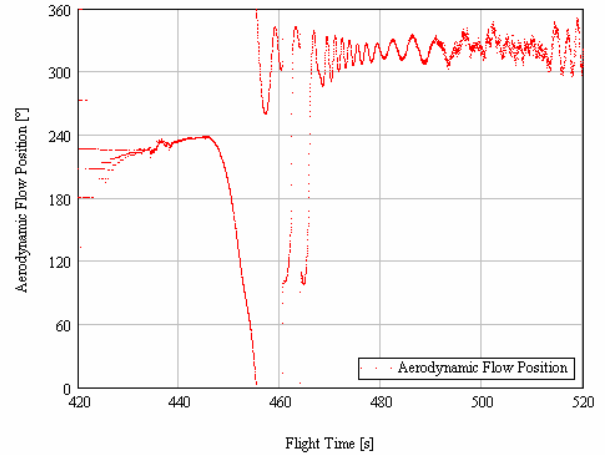

Figure 9. TEXUS-43 – Position of Incoming Flow $Pos_{AeroFlow}$ at the Payload during the Re-entry

The differences in the flow separation, forces the cylindrical payload into a rotational motion about the axis of highest inertial moment when it reaches subsonic velocity [19]. The flat spin rate of the MAXUS-7 payload is shown in Figure 10.
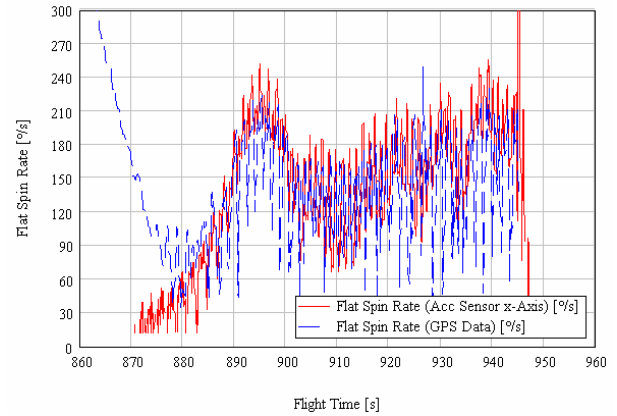

Figure 10. Flat Spin Rate, calculated with GPS and Accelerometer Data

If the payload does not change the velocity in horizontal direction and a perpendicular attitude to the flight vector is assumed, it is possible to calculate the flat spin also with GPS acceleration data.
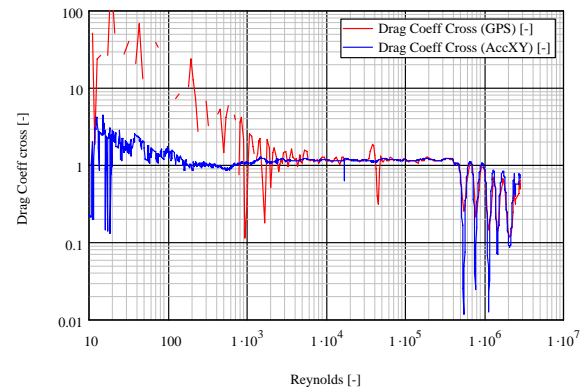

Figure 11. TEXUS-43 – Drag Coefficient $c_{D,\square}$ vs. Reynolds-Number

The calculated drag coefficient $c_{D,\square}$ of TEXUS-43 dependent on the Reynolds-Number *Re* during the re-entry is shown in Figure 11. The payload passes the supercritical Reynolds-Numbers twice during the re-entry and the drop of the drag coefficient that is shown in Figure 5 applies only for subsonic flow regime when the payload passed Mach 1.
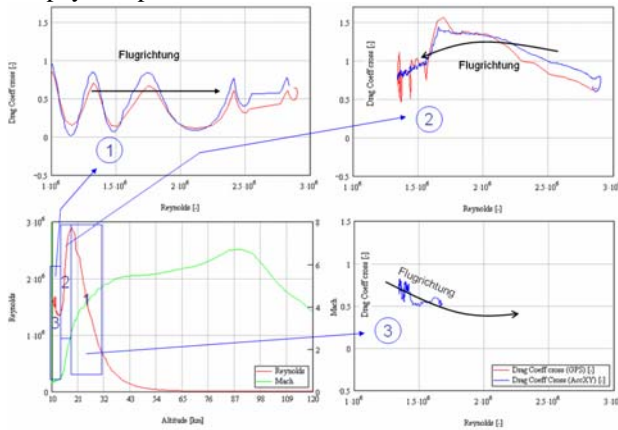

Figure 12. TEXUS-43 – Drag Coefficient $c_{D,\square}$ vs. Reynolds-Number in Supercritical Flow Regime

6. SUMMARY & OUTLOOK

This analysis focused on the similar behaviour of sounding rocket payloads during the re-entry. The drag Coefficient dependence on geometry and Reynolds- and Mach-Number has been shown with real flight data.

This data is not only interesting for a post-analysis of a sounding rocket flight but also for re-entry simulation of future flights. Modelling the re-entry has often been performed by simulating not only the payload position and velocity but also its dynamic attitude motion [17], [19]. The drag coefficient of the vehicle is then calculated depending on its attitude and theoretical value, respectively empirical data from laboratory experiments.

The data that is presented in this paper has been used to build an empirical model that calculates drag coefficient only dependent on geometry, Mach-Number and altitude respectively atmosphere density. Flown payloads have been simulated and the trajectories and interesting events during re-entry have been compared regarding flight time and altitude. An extension on the re-entry prediction will be implemented for the next TEXUS flights.

7. REFERENCES

1. Allen H.J. / Perkins E., *Characteristics of Flow over inclined Bodies of Revolution*, National Advisory Committee For Aeronautics, NACA RM A50L07, 1951

2. Astrium, *MAXUS-4 Flight Preperation and Mission Performance Report*, Astrium GmbH, 2001.

3. Chobotov, *Spacecraft Attitude Dynamics and Control*, Krieger Publishing Company, 1991.

4. Cigada A. / Malavasi S. / Vanali M., *Effects of an asymmetrical confined flow on a rectangular cylinder*, Journal of Fluids and Structures 22, p. 213 – 227, 2006.

5. EADS Space Transportation GmbH, *MAXUS 5 – Flight Preperation and Mission Performance Report*, EADS Space Transportation GmbH, 2004.

6. ESA, *ECSS – Space Engineering – Space Environment*, ESA, 2000.

7. ESA, *ECSS - The Neutral Atmosphere*, ESA, 2000.

8. Jirka G., *Hydromechanik*, Universität Karlsruhe, 2001.

9. Jung W., *TEXUS EML-1Pre-Launch Report,* DLR, RB-MR, 2005-11-29.

10. Jung W. / de Magalhães Gomes R., *TEXUS-43 – Pre-Flight Report,* DLR, RB-MR, 2006.

11. Koppenwallner G., *Einführung in die Satellitenaerodynamik*, Hyperschall Technologie Göttingen.

12. Lamb H., *Hydrodynamics*, University of Cambridge, 1932.

13. Lübken F.-J., *Report on the Meteorological Rocket Flights from Kourou I Conjunction with the Ariane-502 Launch on October 30, 1997*, Physikalisches Institut der Universität Bonn, 1997.

14. McGarvey J., *Recovery of Sounding Rocket Payloads by Center-Of-Gravity Position Control*, American Institute of Aeronautics and Astronautics, AIAA 3rd Sounding Rocket Technology Conference, Albuquerque, New Mexico, 1973.

15. Montenbruck O. / Gill E., *Satellite Orbits* (Springer Verlag, 2000)

16. Pfeuffer H., *TEXUS-43 Post-Flight Review*, Kayser-Threde GmbH, 2006.

17. Ratajczak T., *Programmierung des dynamischen Verhaltens einer rotierenden Raketennutzlast*, Universität der Bundeswehr München, 2001.

18. Stamminger A. / Turner J. / Hörschgen, M. / Jung W., *Sounding Rockets as a Real Flight Platform for Aerothermodynamic CFD Validation of Hypersonic Flight Experiments*, 5th European Symposium on Aerothermodynamics for Space Vehicles, Köln, Nov. 2004.

19. Tong D., *Payload Vehicle Aerodynamics Re-Entry Analysis*, Journal Of Spacecraft And Rockets, Vol. 29, No.5, September-October 1992.

20. Turner J. / Hörschgen M. / Jung W. / Stamminger A. / Turner P., *SHEFEX – Hypersonic Re-entry Flight Experiment – Vehicle Subsystem Design, Flight Performance and Prospects*, AIAA 14th Spaceplane Systems and Technologies Conference, Canberra, 2006.

21. Wille R., *Strömungslehre*, Lecture Material, TU Berlin, 2005.